

Characterization of nanometer-scale defects in metallic glasses by quantitative high-resolution transmission electron microscopy

Jing Li,¹ Z. L. Wang,² and T. C. Hufnagel^{1,*}

¹*Department of Materials Science and Engineering, Johns Hopkins University, Baltimore, Maryland 21218*

²*School of Materials Science and Engineering, Georgia Institute of Technology, Atlanta, Georgia 30332*

(Received 16 November 2001; revised manuscript received 9 January 2002; published 25 March 2002)

Although defects can have a significant effect on the properties of amorphous materials, in many cases these defects are poorly characterized and understood. This is at least partly due to the difficulty of imaging defects in amorphous materials in the electron microscope. In this work, we demonstrate the utility of quantitative analysis of high-resolution transmission electron microscopy for the identification and characterization of nanometer-scale defects in metallic glasses. For a proper identification of such defects, it is important to carefully consider the effects of the imaging conditions and thickness variations in the sample, both of which we describe in detail. As an example, we show that regions of localized plastic deformation (shear bands) in bulk metallic glasses contain a high concentration of nanometer-scale voids. These voids apparently result from the coalescence of excess free volume once the applied stress is removed.

DOI: 10.1103/PhysRevB.65.144201

PACS number(s): 61.72.Dd, 61.43.Dq, 62.20.Fe

I. INTRODUCTION

Transmission electron microscopy (TEM) is one of the most useful tools for studying defects in crystalline metals, with a wide variety of imaging and diffraction modes that can reveal defects such as dislocations. In most cases, these modes make use of the fact that defects create local disruptions in the otherwise perfect periodicity of the crystalline structure. Thus, it is the very existence of a lattice that allows us to detect the defects in the structure. Defects are also important in amorphous materials, but the very fact that these materials are noncrystalline makes the identification and characterization of defects in the TEM quite challenging.

Despite the challenges, some progress has been made towards developing TEM techniques for imaging defects in amorphous materials. In this paper, we report on our use of quantitative high-resolution transmission electron microscopy (HRTEM) to identify nanometer-scale defects in shear bands in bulk metallic glasses, using a technique previously described by Miller and Gibson.¹ Of particular importance is the influence of imaging conditions and variations in sample thickness on the results, which we describe in some detail. We observe a high concentration of defects in shear bands (regions of the metallic glass which have undergone extensive local plastic deformation). We believe the defects form when excess free volume in the active shear band coalesces into voids.

II. SAMPLE PREPARATION AND IMAGING

We prepared 3 mm diameter rods of amorphous $Zr_{57}Ti_5Cu_{20}Ni_8Al_{10}$ by arc melting master alloy ingots from the pure elements, followed by casting into a copper mold. Samples for electron microscopy were prepared by electropolishing sections of the rods in a solution of 30% perchloric acid in ethanol at -30°C for 20–30 s (until perforation). We usually observed that samples electropolished in this way had some residual surface contamination, which we removed by a brief (1 h) ion milling process (3 kV, 0.1–0.25

mA, at 11° incidence). Ordinary handling of the TEM specimens produced small cracks at the edge of the electron-transparent region; ahead of and around these microcracks, shear bands (regions of local plastic deformation) were observed in ordinary bright-field TEM imaging. The contrast in bright-field imaging arises because the deformed regions are thinner than the undeformed material. For the particular example described below, the measured thickness of the undeformed material is approximately 10 nm and that of the shear band region approximately 5 nm. We used a Philips CM300 field emission gun microscope operated at 300 kV; the images were collected on a charge-coupled device (CCD) camera.

III. DATA ANALYSIS

A. Overview of an example of analysis

The analysis procedure we used follows that of Miller and Gibson, who first described its use for identification of nanometer-scale voids in amorphous silica thin films.¹ In this section, we briefly outline the analysis procedure (with comments relevant to our particular case) and provide images of an example. Additional details on several critical points are provided in the following sections.

(1) We begin by obtaining HRTEM images that contain both deformed and undeformed regions in a single micrograph [Fig. 1(a)]. Using a single image ensures that the contrast transfer function (CTF) is the same for both regions, eliminating any effect of the microscope conditions on the comparison of the two regions that might occur if they were imaged separately. For imaging defects in metallic glasses, it is convenient to choose a defocus value of around -200 nm. At this defocus the first zero of the contrast transfer function occurs at about $k = 1.8 \text{ nm}^{-1}$; this allows us to examine the region of interest ($0.5 < k < 1.5 \text{ nm}^{-1}$) without having to worry about the effect of contrast reversal on the image. This is discussed in more detail below.

(2) We then calculate the two-dimensional Fourier transform of two portions of the image, one from an undeformed

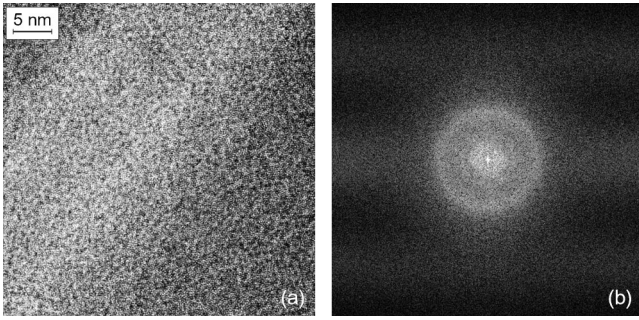


FIG. 1. (a) HRTEM image of a shear band ahead of a crack tip. The shear band is the brighter region that extends across the left-hand side of the image. (b) Two-dimensional Fourier transform of the image in (a).

region and one from a region of plastic deformation. Separate transforms for the two regions are not shown; Fig. 1(b) shows transform of the entire image, used below.

(3) Because there are no strong directional effects, we azimuthally average the two-dimensional transforms to obtain one-dimensional equivalents for each region (using the program FIT2D²), as shown in Fig. 2(a). The one-dimensional transforms for our samples always show a peak near $k = 4 \text{ nm}^{-1}$, corresponding to the amorphous halo, and a second peak at low k , corresponding to small-angle scattering. Although the various features in the ratio are not dramatic, in comparing undeformed and deformed regions, we always observe two systematic differences. First, the peak near $k = 4 \text{ nm}^{-1}$ is always broader for the deformed region, suggesting increased atomic disorder due to plastic deformation. Second, the peak in the small-angle scattering region,

near $k = 1 \text{ nm}^{-1}$, is always more prominent for the deformed region. This suggests that whatever structural features may be responsible for the small-angle scattering exist in greater numbers in the deformed region. These observations from the Fourier transform data agree well with the results of a series of axially aligned dark-field images for the same samples.³

(4) We next take the ratio of the two one-dimensional transforms, dividing the data from the deformed region by that from the undeformed region [Fig. 2(b)]. This ratio should be sensitive to any structural differences between the two regions.¹ In the present case, the ratio is rather noisy due to the small size of the shear band region (which limits the size of the regions which can be Fourier transformed), and because the structural differences between the two regions are small. Nevertheless, we see a peak in the ratio near $k = 1 \text{ nm}^{-1}$, indicating that the peak in the small-angle scattering region is indeed more significant for the deformed region. Although barely larger than the statistical uncertainty in the ratio, we have observed this peak at a variety of defocus conditions and for several different deformed regions. We also observe that the intensity fluctuations in the shear band (described below) are larger, relative to those in the matrix, for spatial frequencies around $k = 1 \text{ nm}^{-1}$ than for other spatial frequencies. We conclude, therefore, that the peak in the ratio near $k = 1 \text{ nm}^{-1}$ is real, and not a statistical anomaly.

This procedure allows us to identify particular ranges of k that correspond to structural features of interest. To actually image the defects giving rise to the enhanced small-angle scattering, we apply a Fourier filtering technique.

(5) Going back to the original HRTEM image (Fig. 1), we perform a two-dimensional Fourier transform of the entire image, including both deformed and undeformed regions [Fig. 1(b)].

(6) Next, we apply an annular filter that passes the spatial frequencies of interest ($0.5 < k < 1.5 \text{ nm}^{-1}$) identified from the ratio, as described in step 4 above. All other spatial frequencies are excluded, which, among other things, eliminates the effects of both contrast reversal and thickness variations on the results. These are critical points, and are described in Sec. III D.

(7) With the filter applied, we do a reverse Fourier transform, to obtain a filtered image [Fig. 3(a)]. Notice that the structural features on this image have characteristic lengths on the order of 1 nm, as a result of the Fourier filtering. The image intensity of this filtered image is related to the projected atomic density, with regions of locally lower density appearing bright and regions of locally higher density appearing dark. Interpreting the image in this way assumes that the weak-phase-object approximation (WPOA) applies, as we discuss in Sec. III B.

(8) Most of the features in Fig. 3(a) merely represent statistical fluctuations in the projected density. To identify actual defects, we apply a threshold filter in which the threshold is set to pass regions which exceed the mean brightness by at least three standard deviations. The result of applying this threshold filter is shown in Fig. 3(b). The spots in this image represent regions with projected densities with statis-

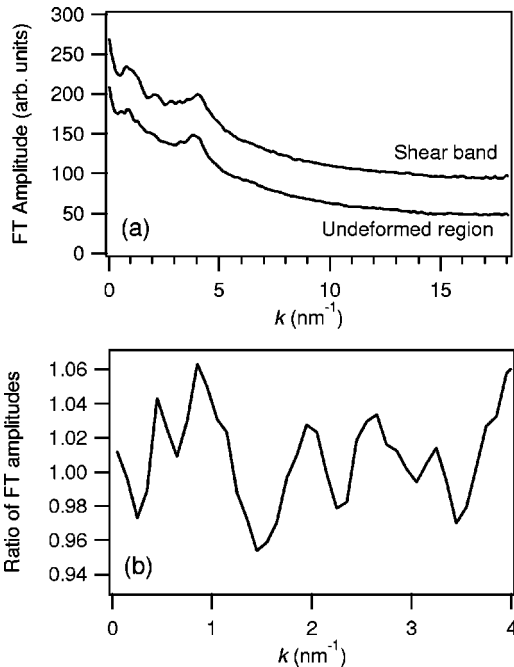


FIG. 2. (a) One-dimensional Fourier transforms of two regions of Fig. 1 (the shear band and undeformed material). The curve for the shear band has been offset vertically for clarity. (b) Ratio of the two one-dimensional transforms from (a).

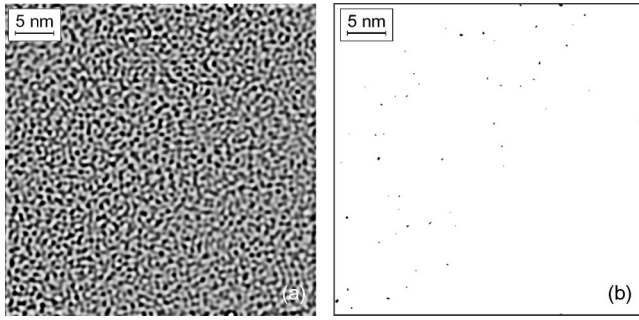


FIG. 3. (a) Same image as Fig. 1(a), Fourier-filtered using a passband of $0.5\text{--}1.4\text{ nm}^{-1}$. (b) Same image as (a), with a threshold chosen to reveal features with brightness three standard deviations greater than the mean. The contrast in this image was inverted for improved reproduction, so that bright features from (a) appear dark here.

tically significantly lower densities than the average. Note that there is a much higher concentration of these features in the deformed region of the sample; as we show below, if the features were the result of simple statistical fluctuations, their apparent concentration would increase with thickness. We observe just the opposite (the deformed region is thinner than the undeformed material), so we conclude that the features in Fig. 3(b) represent true structural defects.

The small spots in Fig. 3(b) serve only to identify which of the features in Fig. 3(a) represent actual defects. The actual size of the defects is obtained from Fig. 3(a), in which the length scale of the features is determined by the range of k space passed by the Fourier filter. From Fig. 3(a) we estimate that the defects are approximately one nanometer in diameter.

The validity of this general approach to identifying defects in amorphous materials has been demonstrated by Miller and Gibson.¹ In the present case, however, three critical issues emerge from the discussion above. First, we consider whether the weak-phase-object approximation applies in the present case and discuss the interpretation of the image contrast. Second, we demonstrate that the ratio technique (step 4) can be used to identify spatial frequencies corresponding to structural features of interest, even if the regions examined are of different thicknesses. Finally, we show that the Fourier filtering technique for identifying defects is still valid, even if there are thickness variations across the sample. In what follows, we take up each of these issues in turn.

B. Validity of weak-phase-object approximation and interpretation of image contrast

In the weak-phase-object approximation, the intensity of a HRTEM image is given by

$$I(x,y) = 1 + 2\sigma\phi(x,y)*s(x,y), \quad (1)$$

where σ is an interaction constant, $\phi(x,y)$ is the projected potential, $s(x,y)$ is a smearing function equal to the Fourier transform of the contrast transfer function, and $*$ indicates a convolution operation.⁴

The condition for the weak-phase-object approximation is that $\sigma\phi \ll 1$, which usually holds only for very thin specimens composed of light elements. For disordered materials, however, the range of thicknesses for which the weak-phase-object approximation applies is greatly extended.⁴ This is because we can add or subtract an arbitrary constant to the phase change $\phi(x,y)$ without affecting the image intensity; in effect, this merely changes the reference point relative to which the phases are measured. In particular, we can write the projected potential as $\phi(x,y) = \phi_0 + \phi'(x,y)$, where ϕ_0 is the average value of the projected potential (presumably directly proportional to the specimen thickness) and $\phi'(x,y)$ represents local fluctuations about the average projected potential. The magnitude of $\phi'(x,y)$ depends on the magnitude of density fluctuations in the specimen, as we discuss below. With this change, the HRTEM image intensity becomes

$$I(x,y) = c + 2\sigma\phi'(x,y)*s(x,y), \quad (2)$$

where c is a constant.

In a crystalline material, with aligned atomic columns, the fluctuations $\phi'(x,y)$ can be quite large and the sample must be very thin to satisfy $\sigma\phi' \ll 1$. For a disordered material, however, the atoms overlap randomly and the fluctuations in the projected potential are quite small relative to the average. A quantitative determination of $\phi'(x,y)$ for the present case would require a detailed model of the atomic-scale structure of our five component glass. While this is the subject of ongoing research, it is beyond the scope of the present study. Instead, we provide some simple observations to show that the weak-phase-object approximation is expected to hold for our samples.

The magnitude of $\phi'(x,y)$ is proportional to the magnitude of the projected atomic density. If $N(x,y)$ is the number of atoms in a column of material, then as a simple approximation it is sometimes assumed that the variation in $N(x,y)$ is given by $\bar{N}^{1/2}$, where \bar{N} is the average value of $N(x,y)$.⁴ This simple approximation predicts much smaller fluctuations than would be observed for a crystalline material, but in fact even it predicts fluctuations that are larger than those actually observed. This is because it assumes that the projected positions of the atoms are randomly distributed. In a real amorphous material, the atomic positions are not uncorrelated; instead, there is short-range order that will make the fluctuations in $N(x,y)$ much smaller than $\bar{N}^{1/2}$. In practice, we typically observe that the fluctuations from an amorphous sample are about one-fourth the size of the fluctuations from a crystalline region of the same thickness. We also observe that a threefold increase in specimen thickness yields an increase of less than 25% in the magnitude of the fluctuations for the amorphous regions. Thus, we conclude that the weak-phase object approximation holds for our amorphous specimens, which are typically 5–10 nm thick.

When interpreting the HRTEM images, we also need to consider the effect of the smearing function $s(x,y)$ in Eq. (2). Under Scherzer defocus conditions, $s(x,y)$ approximates a single, sharp negative peak, so that the image intensity represents the projected potential distribution (which is proportional to the projected density). Because $s(x,y) < 0$, re-

regions of high projected potential [$\phi'(x,y) > 0$] appear dark in the image, while regions of low projected potential [$\phi'(x,y) < 0$] appear bright.

In practice, we use Fourier-filtered images to examine particular length scales of interest. The intensity of an image filtered by the application of an annular mask $M(k)$ is

$$I_f(x,y) = 2\sigma\phi'(x,y) * \text{FT}[\text{CTF} \times M(k)], \quad (3)$$

where CTF represents the contrast transfer function [the Fourier transform of $s(x,y)$].¹ In what follows, we assume that the range of spatial frequencies passed by the annular mask ($k_i < k < k_0$) is entirely within the first zero of the contrast transfer function. This allows us to treat the contrast transfer function as approximately constant, in which case the image intensity is indeed proportional to the projected potential, as discussed below.

With this assumption, the Fourier transform of $\text{CTF} \times M(k)$ is a sharp Gaussian-like peak, which smears the atomic potential but does not introduce significant complexity into the image interpretation. Equation (3) therefore becomes

$$I_f(x,y) \approx 2c\sigma\phi'(x,y), \quad (4)$$

where c is a constant. (Note that in applying the annular mask, we have discarded all of the structural information other than for $k_i < k < k_0$.) Thus, the intensity of the Fourier-filtered image represents the fluctuations $\phi'(x,y)$ in the projected potential $\phi(x,y)$. The effect of different specimen thicknesses on the image will be to change the average intensity, but the filtering process eliminates this, and what we observe are the fluctuations in intensity.

C. Effect of thickness on ratio of Fourier transform amplitudes

The intensity of the HRTEM images is given by $I(x,y)$ from Eq. (2). The amplitude of the Fourier spectrum $\tilde{I}(k)$ is therefore

$$\tilde{I}(k) = I_0 \{ \delta(k) + 2\sigma|\tilde{\phi}(k)| [P^2(k) \times \sin^2\chi(k)]^{1/2} \}, \quad (5)$$

where $\tilde{\phi}(k)$ is the Fourier transform of $\phi(x,y)$, $P(k)$ is a damping envelope caused by microscope instability and limited coherence, and $\sin\chi(k)$ is the contrast transfer function.¹ In Eq. (5), the delta function represents the central spot due to the transmitted beam, while the second term in brackets represents the rest of the spectrum, which is the contribution from scattered beams (modulated by the contrast transfer function).

As above, we write the inner potential $\phi(x,y)$ as the sum of an average potential ϕ_0 and fluctuations $\phi'(x,y)$ about the average $\phi(x,y) = \phi_0 + \phi'(x,y)$. Now we have

$$\tilde{\phi}(k) = \text{FT}[\phi_0 + \phi'(x,y)] \quad (6)$$

$$= \phi_0\delta'(k) + \text{FT}[\phi'(x,y)] \quad (7)$$

$$= \phi_0\delta'(k) + \tilde{\phi}'(k), \quad (8)$$

where FT denotes the Fourier transform of the quantity in brackets. The $\delta'(k)$ term here adds to the intensity of the central spot $\delta(k)$ in Eq. (5). We are interested only in $k > 0$, so we ignore these delta functions in the following development.

If two HRTEM images are taken under precisely the same conditions, the contrast transfer function and the damping envelope are the same for both images, and the ratio of the Fourier spectra $R(k)$ is given by

$$R(k) = \frac{I_1(k)}{I_2(k)} = \frac{2\sigma|\tilde{\phi}_1(k)| [P^2(k) \times \sin^2\chi(k)]^{1/2}}{2\sigma|\tilde{\phi}_2(k)| [P^2(k) \times \sin^2\chi(k)]^{1/2}} = \frac{|\tilde{\phi}_1'(k)|}{|\tilde{\phi}_2'(k)|}. \quad (9)$$

Thus, the ratio of the Fourier spectra for $k > 0$ depends only on the magnitude of the fluctuations $\phi'(x,y)$ in $\phi(x,y)$, and not on the average potential ϕ_0 . Taking the ratio in this way greatly reduces the sensitivity of the technique to variations in sample thickness. The effect of sample thickness is therefore much smaller than in conventional HRTEM. In addition, the fluctuation potential $\phi'(k)$ does not depend very sensitively on sample thickness; this is discussed in more detail in the next section.

D. Effect of thickness on identification of defects

Images such as Fig. 3(b) identify regions in the sample with statistically significant fluctuations in the projected potential, and therefore in the projected density. As we discussed in Sec. III B, the magnitude of the fluctuations $|\phi'(x,y)|$ should increase with increasing sample thickness, and therefore the density of features identified from images such as Fig. 3(b) should also increase with sample thickness. In this section, we provide experimental evidence that demonstrates this effect.

Figure 4(a) shows a HRTEM image from a region near the edge of a hole created during sample preparation. There are no cracks or areas of plastic deformation in this region, so we believe that there are few (if any) defects due to plastic deformation of the type identified in Fig. 3(b). Figure 4(b) shows a Fourier-filtered image of the same region, with the filter chosen to select only the central spot of the two-dimensional Fourier transform. In this filtered image, the image intensity corresponds to the transmitted intensity, so brighter portions of the image correspond to thinner regions of the sample. A fairly uniform increase in sample thickness is apparent as the distance from the edge of the hole increases. Figures 4(c) and 4(d) are Fourier-filtered and thresholded images, respectively, of the same region, this time using the same filtering parameters as the earlier example (Sec. III A) to identify possible defects. From a comparison of Figs. 4(b) and 4(d), it is apparent that as the thickness of the specimen increases, the number of features identified increases. This agrees with the conclusion reached in Sec. III B.

Despite not being subjected to plastic deformation, the region of the sample Fig. 4(d) nevertheless shows many features identified by the filtering and thresholding process. In comparison, the undeformed region of Fig. 3(b) shows few

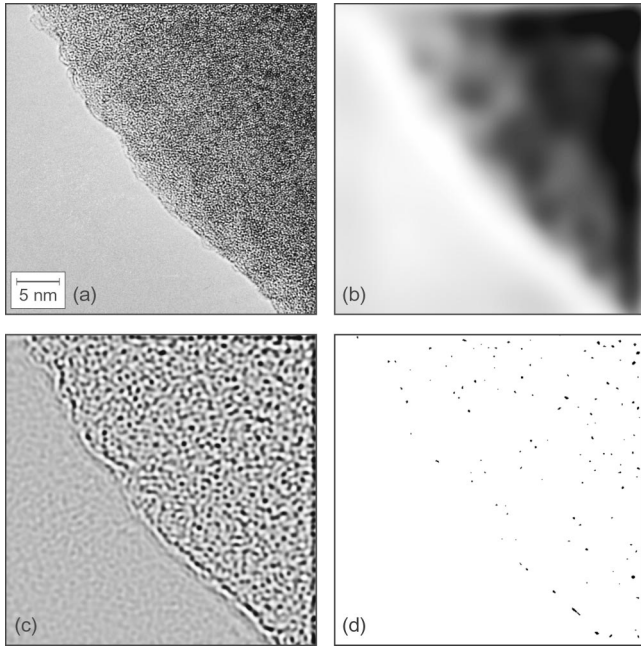


FIG. 4. Four images of an undeformed region of the sample near the edge of a hole. The scale is the same for all four images. (a) HRTEM image. (b) Fourier filtered image, with a filter chosen to only pass the central spot of the Fourier transform. The intensity is related to the thickness of the sample, with thinner areas appearing bright and thicker areas dark. (c) Fourier filtered image, using a passband of $0.5\text{--}1.4\text{ nm}^{-1}$ to reveal features with a length scale of approximately one nanometer. (d) Same image as (c), but with a threshold chosen to reveal features with brightness three standard deviations greater than the mean. Note that thick regions [dark areas from (b)] tend to have more features than thin regions.

such features. The reason for the difference is that although the threshold criterion is the same in each case (three times the standard deviation of the intensity distribution), the standard deviation is larger in the case of the image with the shear band because the fluctuations in the shear band are quite large. If the lower threshold from Fig. 4(d) were applied to Fig. 3(b), we would see approximately the same density of identified features in both (in the undeformed regions).

Thus, we see two differences in identified features between the deformed and undeformed regions of the sample. First, the observed variation in the projected potential (and hence projected density) is larger for the features observed in the shear bands. Second, we observe a much higher concentration of these features in the shear band than in the undeformed material, despite the fact the shear band is thinner than the undeformed material. We conclude that the features apparent in Fig. 3(b) represent true structural defects in the shear band, and are not merely the result of statistical fluctuations in the projected density. Because the observed variations in intensity for the defects is quite large, they must represent regions of significantly lower density than the surrounding material. The most likely explanation is that they are actual voids; if they were merely regions of slightly reduced density, they would not give rise to such large variations in the projected intensity.

Because we are examining regions of different thickness, another potential complication is the effect of attenuation due to absorption. We write an average attenuation factor $\exp(-\mu\phi_i)$, where μ is an absorption coefficient and ϕ_i is the imaginary part of the potential.⁵ Then the transmission function becomes

$$q(x,y) = \exp[-i\sigma\phi'(x,y)]\exp(-\mu\phi_i), \quad (10)$$

where we note that $\phi'(x,y)$ is real. The effect of the attenuation term is to reduce the Fourier amplitude throughout the entire range of spatial frequencies by a constant factor that is a function of specimen thickness. This will not affect the identification of peaks in the ratio of Fourier amplitudes, described above.

The absorption will, however, reduce the amplitude of the intensity fluctuations in the Fourier filtered image. This reduction will be greater for thicker regions of the specimen. As a result, if absorption were a significant effect, we would expect to observe fewer features in the thicker regions of the sample. In fact, however, we observe just the opposite (see Sec. III D). Thus, we conclude that the effects of absorption are small for the range of sample thicknesses studied here.

IV. DISCUSSION

Metallic alloys provide a good example of the differences in properties between crystalline and noncrystalline materials, and the effects of defects in each. In crystalline alloys, plastic deformation is governed by the creation and propagation of dislocations, and their interactions with each other as well as with other defects (such as grain boundaries). Our understanding of dislocation behavior has been greatly enhanced by our ability to observe them in the electron microscope.

In metallic glasses, plastic deformation in shear bands also occurs by the formation and motion of defects. In this case, however, the flow defects are not dislocations, but are thought to be regions of a few nanometers extent of locally higher atomic volume (“free volume”).^{6,7} Direct observation of these defects is a challenging prospect. In an amorphous material, there is no Bragg scattering that can be locally perturbed to allow a defect to be imaged. Furthermore, the expected density variations are quite small ($\sim 1\text{--}2\%$). The existence of increased free volume in plastically deformed metallic glasses has been indicated by recent positron annihilation observations,⁸ but that technique does not have sufficient spatial resolution to investigate individual shear bands in detail.

In the present case, the defects we observe are voids of approximately one nanometer diameter, located primarily in regions of plastic deformation. The existence of such voids in shear bands was inferred by Donovan and Stobbs, on the basis of electron scattering data.⁹ They speculated that if an applied shear stress created excess free volume in a shear band, then when the shear stress was removed the excess free volume would coalesce into small voids. Quantitative high resolution electron microscopy, as described here, allows us to image these voids directly, and obtain quantitative information about their size, numbers, and distribution.

Such quantitative information in turn allows us to begin to understand the formation and behavior of defects. For instance, let us assume that all of the void volume was uniformly distributed as free volume in the active shear band. Based on the size and number density of the voids, we can estimate that the active shear band had approximately 0.4% more volume per atom than the undeformed material. This is comparable to the change in volume associated with structural relaxation of a metallic glass due to annealing.¹⁰ Furthermore, we can also demonstrate, quantitatively, that the coalescence of the voids is a thermodynamically favorable process. This is because the free energy reduction due to lowering the free volume in the shear band is more than enough to offset the surface energy cost associated with the formation of the voids.¹¹

We believe that techniques described here can be extended to obtain even more detailed information about the defects. For instance, by a suitable choice of Fourier filters, it should be possible to estimate not only the average size but the size distribution of the voids. Such information could be very useful for determining the mechanism of void nucleation.

V. CONCLUSIONS

We have shown that quantitative high resolution transmission electron microscopy can be usefully applied to the study of defects in bulk metallic glasses. So long as the weak-phase object approximation holds for the fluctuation component of the projected potential, the image intensity is proportional to the projected atomic density. By suitable Fourier filtering and image thresholding techniques, regions of atomic density significantly lower (or higher) than the average can be identified. We observe a large concentration of nanometer-scale voids in shear bands, which we suggest are the result of the coalescence of excess free volume in the active shear bands into voids when the applied shear stress is removed.

ACKNOWLEDGMENTS

We gratefully acknowledge K. Livi for assistance with the TEM imaging, X. Gu for sample preparation, and fruitful discussions with Y. Ding, P. Voyles, J. M. Gibson, F. Spaepen, and R. C. Cammarata. This research was supported by the U. S. Army Research Office under Grant No. DAAG55-98-1-0487 and the National Science Foundation under Grant No. 9875115.

*Electronic address: hufnagel@jhu.edu

¹P.D. Miller and J.M. Gibson, *Ultramicroscopy* **74**, 221 (1998).

²A.P. Hammersley, *FIT2D: An introduction and overview*, 1997.

³J. Li, X. Gu, L.-Q. Xing, K. Livi, and T. C. Hufnagel, in *Supercooled Liquid, Bulk Glassy and Nanocrystalline States of Alloys*, edited by A. Inoue, A.R. Yavari, W.L. Johnson, and R.H. Dauskardt, MRS Symposia Proceedings No. 644 (Materials Research Society, Pittsburgh, 2001), p. L12.19.

⁴J.M. Cowley, in *High-Resolution Transmission Electron Microscopy and Associated Techniques*, edited by P. Buseck, J. Cowley, and L. Eyring (Oxford Science Publications, Oxford, 1992), pp. 3-37.

⁵J. M. Cowley, *Diffraction Physics* (North-Holland, New York, 1986).

⁶P.S. Steif, F. Spaepen, and J.W. Hutchinson, *Acta Metall.* **30**, 447 (1982).

⁷A. Argon, *Acta Metall.* **27**, 47 (1979).

⁸K.M. Flores, Daewoong Suh, R. Howell, P. Asoka-Kumar, P.A. Sterne, and R.H. Dauskardt, *Mater. Trans., JIM* **42**, 619 (2001).

⁹P.E. Donovan and W.M. Stobbs, *Acta Metall.* **29**, 1419 (1981).

¹⁰A. L. Greer, in *Rapidly Solidified Alloys*, edited by H. H. Liebermann (Marcel Dekker, New York, 1993), pp. 269–301.

¹¹J. Li, F. Spaepen, and T. C. Hufnagel (unpublished).